1A.2 A DETAILED LES STUDY OF TRANSPORT AND MIXING NEAR CLOUD EDGES

Susan Pesman and Harm J. J. Jonker*
Multi-Scale Physics, Delft University of Technology, The Netherlands

ABSTRACT

In recent studies (Jonker et al. [2008], Heus et al. [2009]) it was found that most of the upward and downward mass transport in shallow cumulus cloud fields occurs near the edge of clouds. This appears to contradict the idea that most mass transport occurs in the buoyant cores of large clouds. To address these and other issues, in this study we make a detailed analysis of Large Eddy Simulations of cumulus clouds with a focus on the cloud edge region. Apart from diagnosing the mass flux as a function of distance to the nearest cloud edge as done previously, we now also simultaneously measure the size of the cloud in order to learn whether the mass transport is dominated by the cores of many small clouds, or by the wide perimeter region of a few large clouds, or by intermediate sized clouds. As the edge region features strong mixing and is responsible for the generation of the descending 'shell' of air surrounding the cloud, we also study the lateral size of cloud shells and test whether or not shell-sizes scale with cloud-sizes. Next we diagnose cloud entrainment properties as a function of distance to cloud edge and verify whether the inner core regions of large clouds entrain relatively less as would be expected from the fact that this region is fenced off from the dry environment. This information relates directly to the notion of 'undiluted cores'. Finally we focus on the local mixing fractions χ of conserved variables such as total specific humidity and liquid potential temperature, and investigate whether χ can be expressed at arbitrary locations as a linear mixture of cloud(-core) properties and environmental properties. Since we know the distance (r) to cloud edge as well, we are able to establish a straightforward relation between geometric properties (r) and mixing properties (χ).

1. INTRODUCTION

Jonas [1990] was one of the first to draw attention to the descending shell of air around active (growing) clouds in aircraft observations. The entrainment of air is influenced by the presence of a shell of subsiding air. Since he observed from droplet spectra that large drops being brought down from higher levels did not significantly evaporate, he concluded that this downdraught must be a result of some mechanical forcing, a pressure gradient for instance. Rodts et al. [2003] also used aircraft observations to investigate the behaviour of the virtual potential temperature and the total water content around the cloud edges and how this influenced the vertical velocity. In this research many cloud transects were averaged after being rescaled to unit length. Based on the results for the virtual potential temperature and the total water content, Rodts et al. [2003] argued that evaporative cooling is the mechanism behind the descending shell rather than the pressure gradient. He was not able to draw any conclusions on the role of the other terms in the vertical momentum budget in the shell region, such as mixing and shear. Heus and Jonker [2008] investigated the behaviour of these other budget terms separately by means of Large Eddy Simulations. They concluded that indeed buoyancy is the driving force behind the descending shell of air and that the pressure gradient (just as the other terms) is even counteractive. Since a lot seems to happen around the edges of a cloud, Jonker et al. [2008] implemented an alternative way of looking at the cloud edge by putting the edge central rather than the cloud center. This method evades the need to rescale clouds before averaging. Based on their LES results they proposed a refined view of vertical mass transport by shallow cumulus clouds, where most – if not all – of the downward mass-flux occurs near the edges of clouds rather than via a uniform descending motion. They also showed that most of the upward mass-flux happens near the edges and not so much in the (geometrical) core of clouds. In this study the area where most of the upward and downward mass flux is located, is called the cloud edge region.

It could be argued that the mass-flux peaks (both upward and downward) near the edge of the clouds are due to the positive buoyant cores of many small clouds. This can be contrasted with the view where the peaks are mainly due to the wide perimeter of the large clouds in the ensemble. This question will be addressed in detail in this study. Another question is what determines the size of the shell. Does the lateral size of the shell scale with the size of the cloud or is this a fixed value? This and the correlation between the strength of the shell and the size of the cloud are investigated as well.

Since mixing and the descending shell appear to be closely related, it is appropriate to look at this mechanism in detail. How does the cloud mix with the far environment?

2. CLOUD EDGE AREA DIAGNOSTICS

2.1 *Cloud Edge Toolbox*

The method of Jonker et al. [2008] to study (thermo)dynamic fields with respect to cloud edges is illustrated in figure 1.

First the points $m = -1$ and $m = 1$ are found around the edge of the cloud. An edge is defined as the position where in one box no liquid water is found ($q_l = 0$) and in its neighbouring box liquid water is present ($q_l > 0$).

**Corresponding author address:* Harm Jonker, Dept. of Multi-Scale Physics, Delft University of Technology, Delft, The Netherlands (h.j.j.jonker@tudelft.nl - www.msp.tudelft.nl)

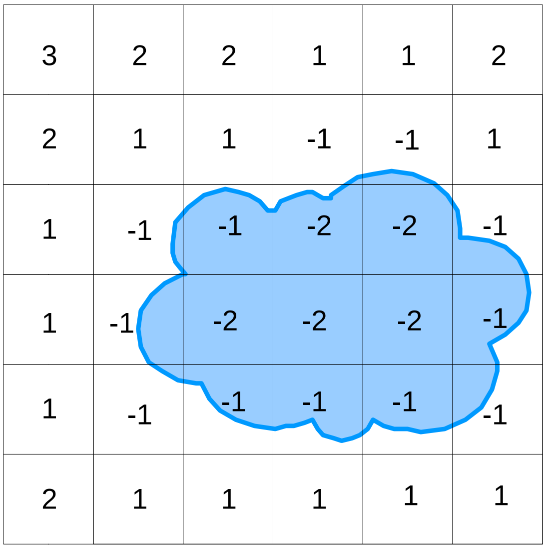

FIG. 1: Illustration of the method determining the distances to the cloud edge. The width of one box is dx

When these are all distributed over the entire domain the points around it are located and are given the number $m = -2$ when it is next to a -1 and the number $m = 2$ when it is found to be next to a number $m = 1$. This process is repeated until the entire domain is filled with numbers, which indicate the distance to an edge of a cloud. The distance can be calculated in meters [m] according to:

$$r = \begin{cases} (m + 0.5)\text{dx} & \text{if } m < 0 \\ (m - 0.5)\text{dx} & \text{if } m > 0 \end{cases} \tag{1}$$

Conditional sampling Besides this common definition of a cloud, which means the presence of liquid water, alternative sampling criteria can be used. An overview of criteria that are used in this research can be found in table 1.

Table 1: Used conditional sampling criteria

Indicator	Type	Sampling criteria
I_1	Cloud	$q_l > 0$
I_2	Cloud updraft	$q_l > 0$ & $w > 0$
I_3	Cloud buoyant core	$q_l > 0$ & $\theta_v > \overline{\theta_v}$

With these criteria the values inside the cloud can be calculated by using the indicator function I_s, with $I_s = 1$ when the corresponding criterion is met and $I_s = 0$ otherwise.

$$\varphi^c = \frac{\int I_s \varphi dA}{\int I_s dA} \tag{2}$$

2.2 *Atmospheric Quantities*

Here the common atmospheric quantities are written as a function of the distance to the cloud edge r.

When all points are located at a certain distance from the cloud, the averaged information at that distance at a certain height can be found according to:

$$\widetilde{\varphi}^{\,r}(r,z) = \frac{L^{-2}\iint \varphi(x,y,z)\delta(\mathbf{r}(x,y,z) - r)dxdy}{n(r,z)} \tag{3}$$

with δ the Dirac function and L the domain size, and $n(r)$ the normalized number of points. These number of points are normalized according to:

$$\int_{-\infty}^{+\infty} n(r)\,dr = 1 \tag{4}$$

How this looks like as a function of the distance to the cloud edge can be found in figure 2.

The value $\widetilde{\varphi}^r$ is the average of φ on a certain distance r from the cloud edge. When not the average but the sum of φ at one distance from the cloud edge is observed then the following notation is used: $\widetilde{\varphi}^r \cdot n(r)$.

For the vertical fluxes equation (3) is used as well, where φ has to be substituted by $w'\varphi'$. Also, the subgrid contributions are taken into account.

2.3 *Decomposition of the Cloud Edge Area*

Vertical momentum budgets When determining which mechanism is the driving force behind the descending shell, the vertical momentum prognostic equation is important. This can be decomposed into separate budgets:

$$\begin{aligned} \frac{\partial w}{\partial t} &= A + B + P + D \\ &= -u_j \frac{\partial w}{\partial x_j} + g\frac{\theta_v}{\Theta_0} - \frac{1}{\rho_0}\frac{\partial p}{\partial z} \\ &\quad + \frac{\partial}{\partial x_j}\left[K_m\left(\frac{\partial u_j}{\partial z} + \frac{\partial w}{\partial x_j}\right)\right] \end{aligned} \tag{5}$$

in which the Coriolis force is neglected, A is the resolved advection term, B is the buoyancy force term, P is the vertical pressure gradient term and D is the parametrized unresolved subgrid diffusion term. This can be further derived according to:

$$\begin{aligned} \frac{\partial w}{\partial t} &= A - \overline{A} + B - \overline{B} + P - \overline{P} + D - \overline{D} \\ &= \underbrace{-u_j \frac{\partial w}{\partial x_j}}_{A} \underbrace{+ g\frac{\theta_v - \overline{\theta_v}}{\Theta_0}}_{B'} \underbrace{- \frac{1}{\rho_0}\frac{\partial p'}{\partial z}}_{P'} \\ &\quad \underbrace{+ \frac{\partial}{\partial x_j}\left[K_m\left(\frac{\partial u_j}{\partial z} + \frac{\partial w}{\partial x_j}\right)\right]}_{D} \end{aligned} \tag{6}$$

With this equation the results by Rodts et al. [2003] and Heus and Jonker [2008] as presented in the introduction can be verified.

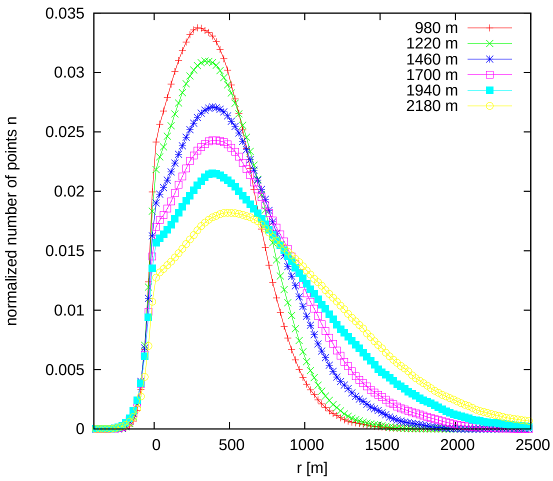

(a) Normalized number of points n

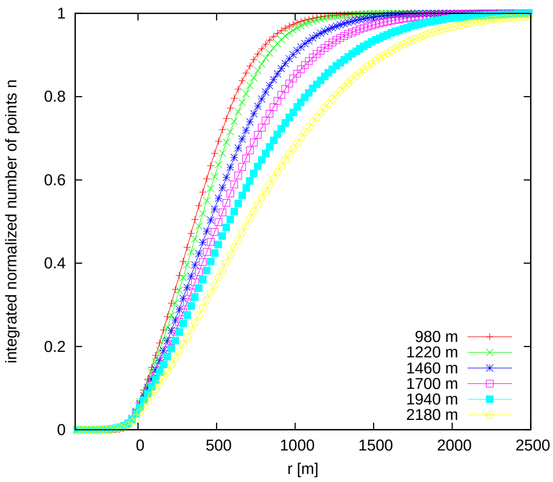

(b) Integrated number of points $\int n(r)dr$

FIG. 2: Illustration of the number of points as function of height z and distance to cloud edge r

Percentage positive buoyant and updraft points When the peak of the mass flux profile is due to buoyant cores it is interesting to take a look at how many points of the total points are actually positively buoyant, as a function of the cloud distance r. To check how this is correlated to the updraft or downdraft profiles also the percentage updraft is calculated as a function of r.

Cloud sizes Due to the fact that all clouds of all sizes are included in this method, it can be argued that the mass flux peak as shown by Jonker et al. [2008] is a consequence of the rising *cores* of many small clouds, since this peak is located so close to the edge. It can also be explained as the consequence of the large perimeters of the biggest clouds. This balance is illustrated in figure 3.

To be able to investigate which one is the case, a different way of decomposing the cloud edge area is

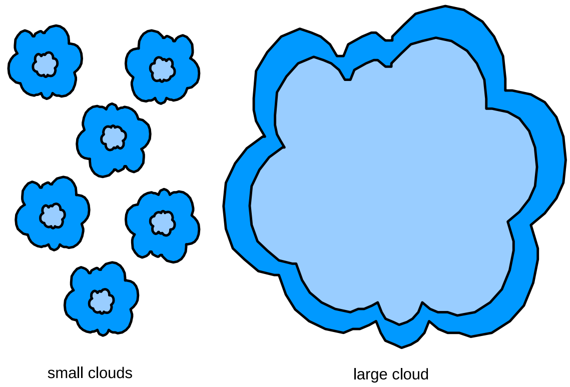

FIG. 3: Views on vertical mass transport: by the cores of many small clouds or the large perimeter of a few large clouds.

needed. A method to select clouds on the basis of their size is the appropriate way. A code is implemented that numbers the individual clouds and calculates their areas A on the x-y-plane at every height. The cloud at that height is then categorized on the basis of its typical size l, according to:

$$l_p = \sqrt{A_p(z)} \tag{7}$$

with p the number of the cloud and z the height.

2.4 *Cloud Edge Area Dimensions*

To find out what sets the dimension of the shell (the strength as well as the width) the same cloud size toolbox is used as introduced in the previous section, to see what the correlation is between the cloud size and the dimensions of the cloud edge region. The width r_{shell} is taken at the point where the vertical velocity w is less than 5% of w_{min} for the first time. The strength of the shell is defined by the value of w_{min} and the width by r_{shell}. Another interesting correlation might be, whether the strength of the peak inside the cloud, w_{max} is correlated with the cloud size. If this is the case, then also something can be said about the correlation of w_{max} with w_{min}. In figure 4 all these values are defined.

A different approach to see whether it is the cloud size that sets the dimensions of the cloud edge area is by scaling the distance r and the velocity w with the cloud size l, according to:

$$w \sim l^{\alpha} \tag{8}$$

where α has to be found. When the graphs for every cloud size lie on top of each other the data collapses and the height / width is scalable by the cloud size, and thus correlated in a certain way.

2.5 *Properties of the Geometric Core*

It is sometimes suggested that the processes in the center of a cloud are adiabatic. In this study the center of the cloud is called the "geometric core", not to be confused with the buoyant core, which is defined in table 1.

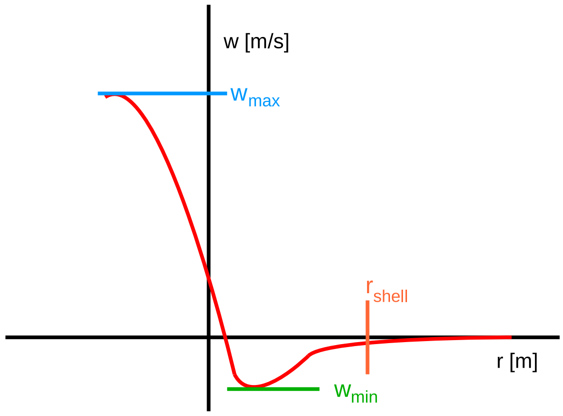

FIG. 4: Definition of w_{max}, w_{min} and r_{shell}

To research this the cloud edge region diagnostics are used to look at the vertical profiles of quantities at certain distances r to the cloud edge. The quantities q_t and θ_l are conserved in adiabatic processes, so their profiles should show a straight vertical line in the geometric core, if it were adiabatic. In adiabatic cases, the profile of θ_v in the core should be parallel to the wet adiabatic lapse rate:

$$\Gamma_m = \Gamma_d \left[\frac{1 + \frac{q_s L_v}{R_d T}}{1 + \frac{L_v^2 q_s}{c_p R_v T^2}} \right] < \Gamma_d \tag{9}$$

Another hint that might lead to the proof of the existence of the so-called “undiluted” cloud cores, is when the entrainment rate approaches zero near this core. Here as a function of r and height z, separately:

$$\varepsilon(z) = \frac{\frac{d}{dz} q_t(r,z)}{q_t(r,z) - q_t^e(z)} \tag{10}$$

2.6 *Cloud Mixing*

The mixing factor χ is used to describe the mixing between the cloud and its environment. We can rewrite χ as a function of r according to:

$$\chi(r) = \frac{q_t^c - q_t(r)}{q_t^c - q_t^e} \tag{11}$$

$$\chi(r) = \frac{\theta_l^c - \theta_l(r)}{\theta_l^c - \theta_l^e} \tag{12}$$

The following definition is used for these calculations:

$$\varphi^c = \varphi(r_{min}) \qquad\qquad \varphi^e = \varphi(r_{max}) \tag{13}$$

thus by taking the deepest and furthest value available.

When a correlation can be found between the mixing ratio χ and cloud distance r, it is possible to try to reconstruct q_l and θ_v with this correlation.

$$q_t(\chi(r)) = \chi(r) q_t^e + (1 - \chi(r)) q_t^c \tag{14}$$

$$\theta_l(\chi(r)) = \chi(r) \theta_l^e + (1 - \chi(r)) \theta_l^c \tag{15}$$

$$q_l(\chi(r)) = q_l^c + \frac{\chi(r)}{1 + \frac{L_v}{c_p} \frac{dq_s}{dT}|_{T^c}} \left[(q_t^e - q_t^c) - \pi(\theta_l^e - \theta_l^e) \frac{dq_s}{dT} |_{T^c} \right] \tag{16}$$

$$\theta_v(\chi(r)) = \left(\theta_l(\chi(r)) + \frac{L_v}{c_p \pi} q_l(\chi(r)) \right) (1 + \epsilon_2 q_t(\chi(r)) - \epsilon_3 q_l(\chi(r))) \tag{17}$$

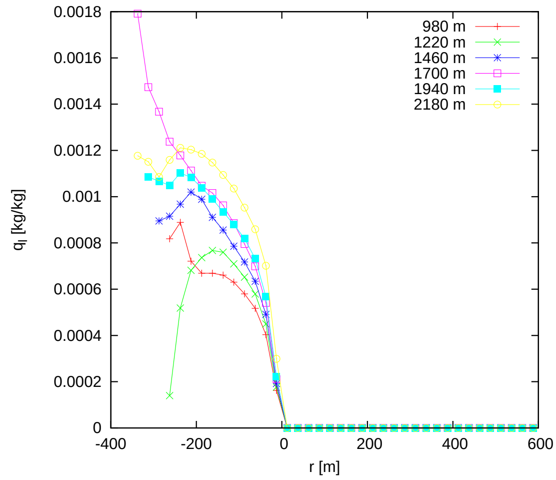

(a) Liquid water content $\widetilde{q_l}^r$

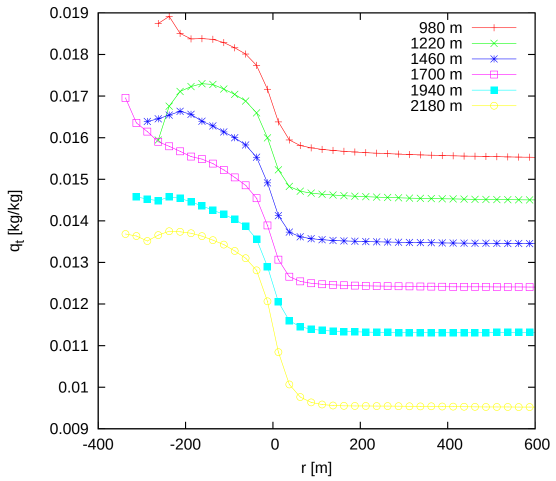

(b) Total water content $\widetilde{q_t}^r$

FIG. 5: Water contents as a function of the distance to the cloud edge

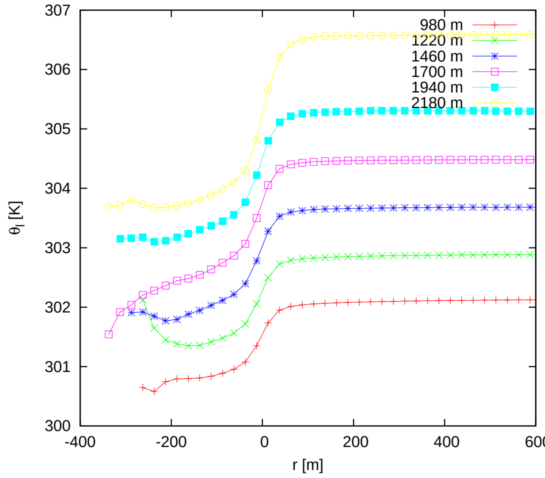

(a) Liquid potential temperature $\widetilde{\theta_l}^r$

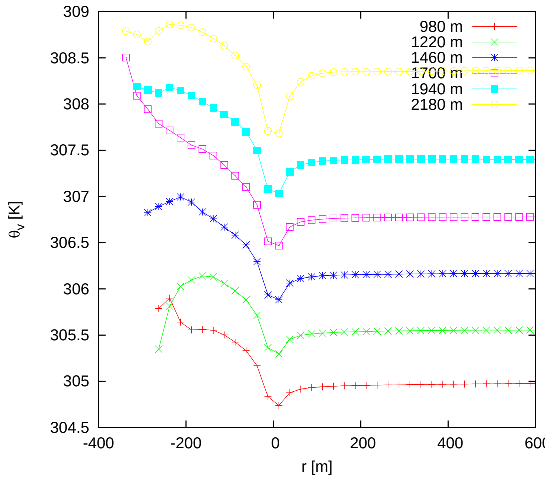

(b) Virtual potential temperature $\widetilde{\theta_v}^r$

FIG. 6: Potential temperatures as a function of the distance to the cloud edge

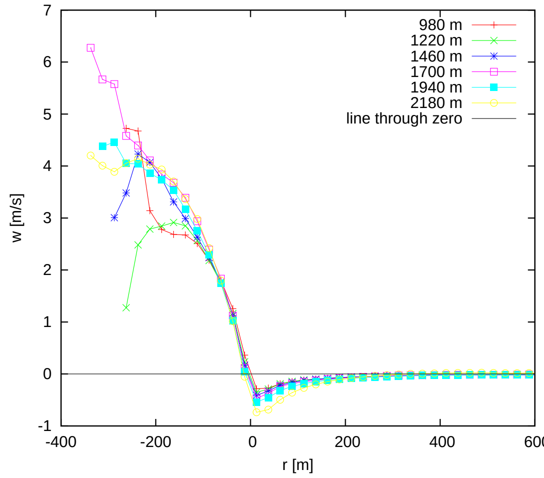

(a) Vertical velocity $\widetilde{w}^r$

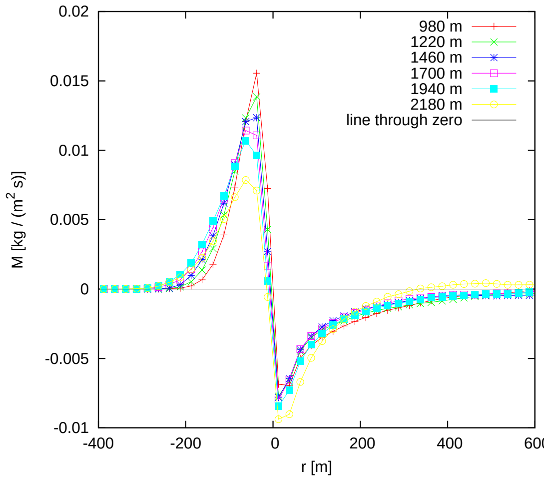

(b) Mass flux contribution M^r

FIG. 7: Vertical velocity and mass flux plotted against distance to cloud edge r

3. RESULTS

3.1 *Atmospheric Quantities*

Mean quantities versus the cloud distance Interesting atmospheric quantities to be analysed in the manner outlined above are the liquid water content q_l, the total water content q_t, the liquid water potential temperature θ_l, the virtual potential temperature θ_v, the vertical velocity w and the mass flux contribution $M(r) = n(r)\tilde{w}^r$. These quantities are shown for various heights in figures 5–7. For these pictures the cloud condition is used for the sampling, as one can observe from the liquid water content, figure 5(a). Another thing to observe for q_t is "the higher, the dryer". For the potential temperatures (figures 6(a) and 6(b)) the opposite behavior is observed. When higher in the atmosphere these values rise, which can be expected when looking at their definitions. Around cloud edge there is a dip in the value for θ_v.

When looking at the figures for $q_t(r)$ and $\theta_v(r)$ we already see an indication that the shell is driven by evaporative cooling, similar to the findings of Rodts et al. [2003], because of the dip near the edge for the virtual potential temperature and the absence of one in the total water content. For the mass flux we observe the same behavior as Jonker et al. [2008] did. Also the downdraught shell can be seen in figure 7(a). Comparing this with the observational results by Wang et al. [2009] shows similar behaviour.

3.2 *Decomposition of the Cloud Edge Area*

First of all we will decompose the region around the cloud edge into different vertical momentum budgets to see what causes the descending shell. Secondly, the turbulence kinetic energy budget terms are shown separately to see where the turbulence is created or destroyed and where it is transported to or from. Finally, the mass flux will be decomposed based on cloud sizes.

Vertical Momentum budgets To see what makes the air go down around a cloud, the separate vertical momentum budgets as described before are plotted, and shown in figure 8. If the influence of lateral mixing is negligible within the shell and the descending air results from a mechanical forcing, we should observe this through a negative pressure gradient in the shell. In this case buoyancy will play a inferior role. On the other hand, when the lateral mixing causes evaporative cooling, we should observe negatively buoyant air around the edge of a cloud, since negative buoyancy is the major driving force behind downward motion. As one can see clearly in these graphs, the only budget contributing to a downward mass flux is the buoyancy force. This is in line with earlier results from Rodts et al. [2003] and Heus and Jonker [2008]. This indicates that lateral mixing is of significant importance around the cloud edge.

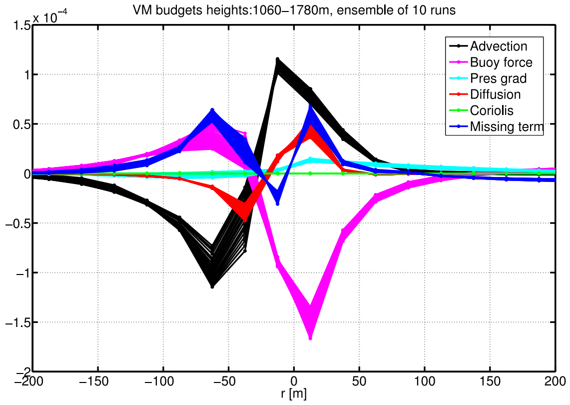

(a) Vertical momentum budgets nA, nB', nP' and nD

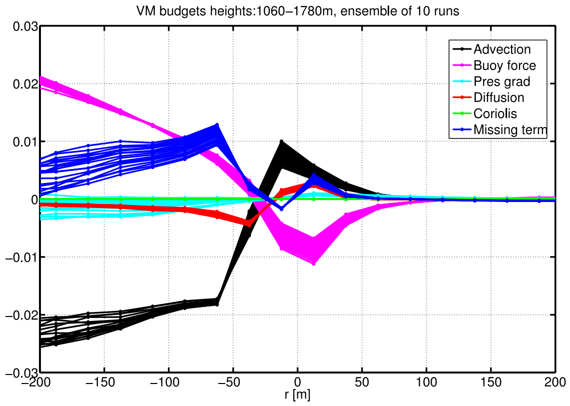

(b) Vertical momentum budgets A, B', P' and D

FIG. 8: Vertical momentum (VM) budgets

What might strike the reader is the unbalance of the terms A, B, P and D. This is caused by the conditional sampling. The clouds grow and shrink in time, which is represented by the "missing term". The balance was checked by measuring the vertical velocity field at some time $t = t_0$ and at $t = t_f$ and checking that the time derivative of the vertical velocity is indeed zero:

$$\frac{\partial w}{\partial t} = \frac{w(t_f) - w(t_0)}{t_f - t_0} = 0 \tag{18}$$

It is nice to see in figure 8(b) how big influence the buoyancy force has on average inside the cloud, with the advection as the main counteractive term.

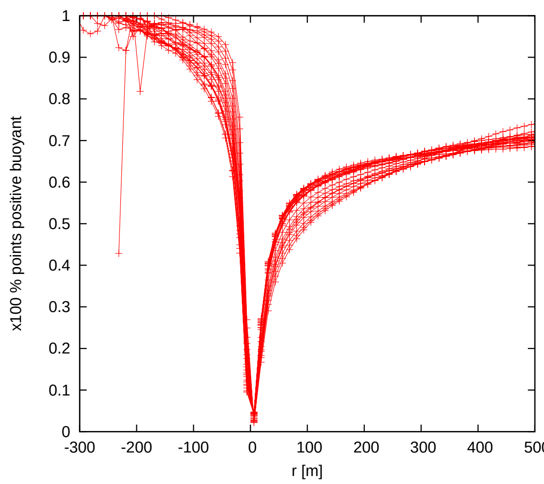

(a) Percentage positive buoyant points

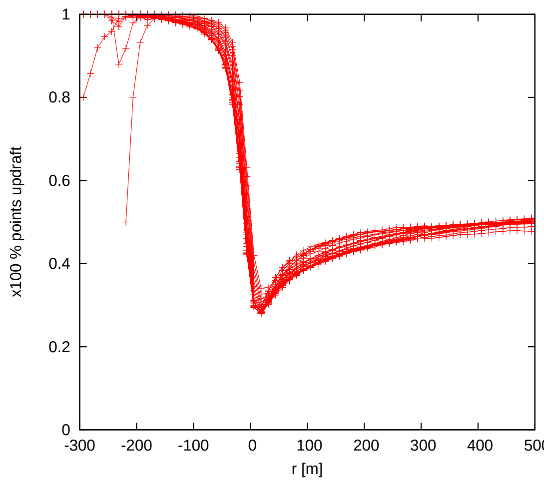

(b) Percentage updraft points

FIG. 9: Percentage buoyant and updraft points

Percentage positive buoyant and updraft points Figure 9(a) shows the percentage positive buoyant points as a function of distance to cloud edge. The percentage of positive buoyant points is almost everywhere above 80% inside the cloud. Only very close to the edge the percentage decreases rapidly. Inside, it rapidly goes to 100% which makes the assumption of buoyant cores reasonable.

Another interesting point in this figure is the fact that in the environment the percentage rises again to about 75%, which means that the environment is on average positive buoyant. This is in contradiction with the idea that the environment is on average neutrally buoyant. Clearly most of the negatively buoyant points reside in the shell region.

In figure 9(b) it can be observed that in the shell the percentage updraft points is low, as expected. Again, it rises when further away from the cloud, to about 50%, which indicates that the environment neither rises or descends on average.

Cloud sizes Another way to investigate the composition of the mass flux peak is by implementing the cloud size statistics as described in section 2.3. The area near the cloud edge is decomposed on the basis of the size l of the cloud. The question is whether the balance will lean towards the large perimeters of the few big clouds or to the cores of the numerous small clouds. In figure 10 it can be seen that the peak is composed of the perimeters of the medium-sized clouds. This means that indeed most of the mass flux occurs in the area around the cloud edges, since the peaks are around $r = -50$ [m] and not at the center of intermediate-sized clouds. Notable in this figure is the fact that all peaks are no deeper inside the cloud than this 50 [m]. For smaller clouds the peaks are closer to the edge, which underpin the thought that the mass flux peak is constructed by the perimeters of clouds. When comparing this figure with figure 9(a) it can be noticed that the buoyant core includes most of the mass flux.

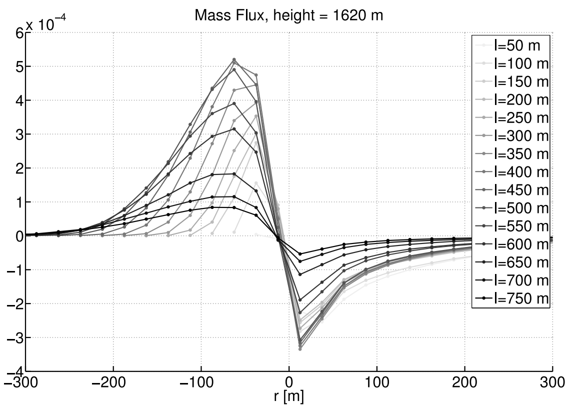

FIG. 10: Mass flux in [m s^{-1}] per cloud size l versus r at z = 1620 m, ensemble average of 10 runs

3.3 *Cloud Edge Area Dimensions*

Now that the tools are available to look at the properties for clouds with different sizes, it is interesting to investigate what sets the size of the shell. With this size the width as well as the strength are meant. With this method available the distance r can be scaled with the cloud size. When this is done and all mass flux peaks seem to have the same width, it means the mass flux is scalable with the cloud size. This graph can be found in figure 11(a). It appears that the peak inside the cloud is reasonable scalable with the cloud size. But the negative peak outside is not collapsing with this scaling. The same can be observed for the vertical velocity, figure 11(b). The negative peak is located on different r values for different cloud sizes.

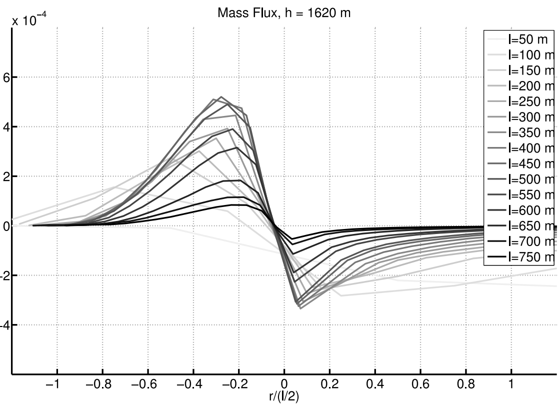

(a) Mass flux in [m s^{-1}] per cloud size

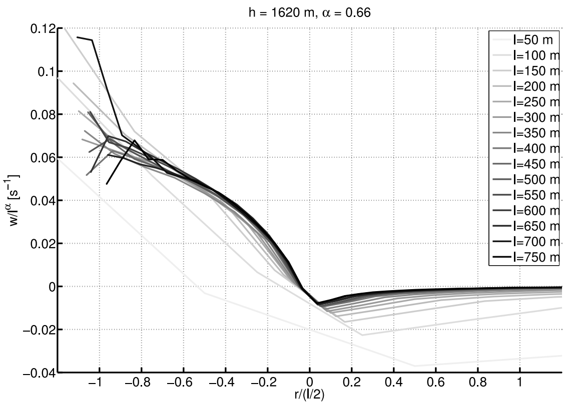

(b) Scaled vertical velocity per cloud size

FIG. 11: Mass flux and vertical velocity figures as function of $2r/l$ at z = 1620 m, ensemble average of 10 runs

The maximum value of the vertical velocity w_{max} does seem to collapse at a certain scaling factor l^{α}, where $\alpha \approx 2/3$. This leads to the thought that not the shell width is set by the size of the corresponding cloud, but maybe only the strength, both inside and outside the cloud. So the correlations of width and strength with cloud size are investigated on the heights in the middle of the cloud, because near cloud base and near the inversion other effects have to be taken into account. The red line in these graphs represents the average of these points. For the strength (figure 12) there appears to be a nega-

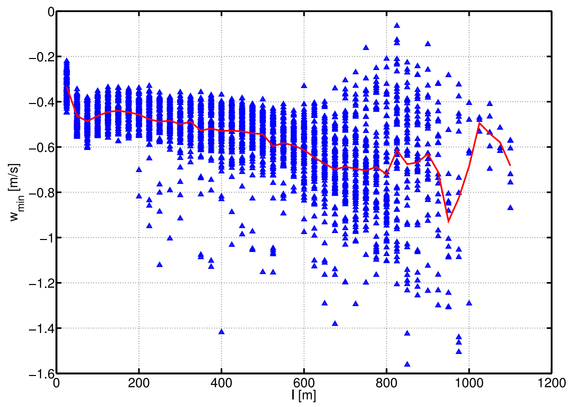

(a) Correlation between the size of the cloud l and the strength of the shell w_{min}

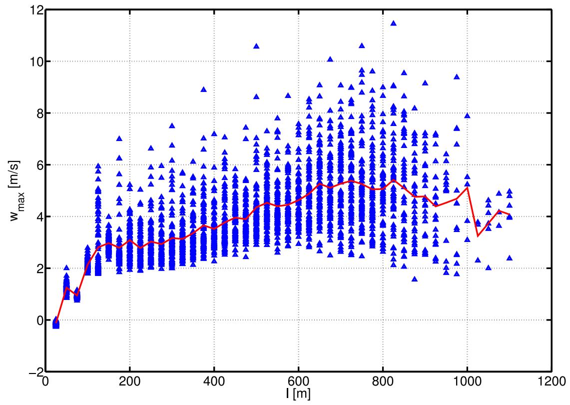

(b) Correlation between the size of the cloud l and the strength of the core w_{max}

FIG. 12: Correlation of the size of the cloud l with the strength of the shell and the core

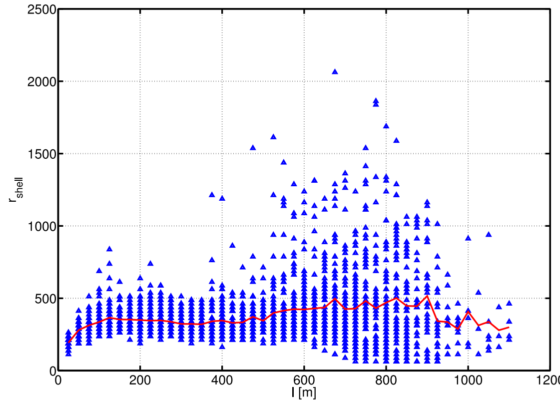

FIG. 13: Correlation of the size of the cloud l with the width of the shell r_{shell}

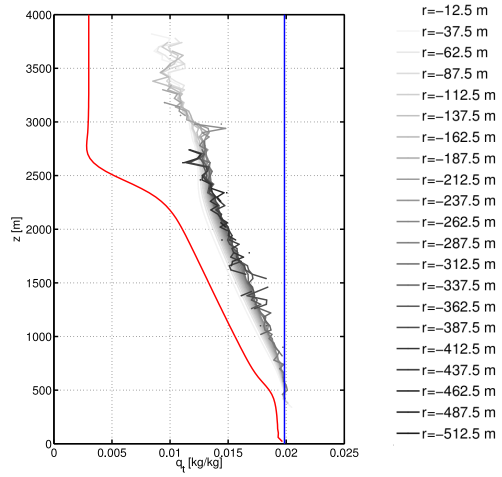

(a) Profile of q_t for different r

FIG. 14: Total water profile for various values of distance to the cloud edge r. The red and blue lines represent the environmental and adiabatic profiles, respectively.

tive correlation, though very weakly. Also, w_{max} versus the cloud size is plotted to see if the strength inside the cloud is correlated in the same way as the strength of the shell with the cloud sizes. Similar behavior can be observed. This implies that when a cloud has a stronger geometric core it also has a stronger negative shell.

For the width, figure 13, a horizontal line can be observed, with just a slight increase for the smaller clouds. This implies that the shell width is independent of the corresponding cloud size.

3.4 *Properties of the Geometric Core*

It is sometimes believed that in the middle of a large cloud the processes are adiabatic and thus undiluted. With the cloud edge diagnostics we can study whether this is true for the shallow convection case considered here. The $\bar{\varphi}^r$-profiles can be plotted for various locations in the cloud with respect to the edge distance. When deep inside the cloud the profiles match the adiabatic profiles, described in 2.5, the cores are undiluted.

All the profiles give the same message. Only just above cloud base the processes could be considered undiluted. But higher up, the lines are start to deviate from the adiabatic profiles for all distances from cloud edge. The closer to cloud edge the earlier (lower) it deviates. But even the profiles deep inside the clouds deviate at some height. This means that deep inside the cloud dilution by mixing is significant.

Another way to confirm this observation is by looking at the entrainment rate of, for instance, the total water content q_t. Entrainment rate profiles for different distances from the cloud edge can be found in figure 16.

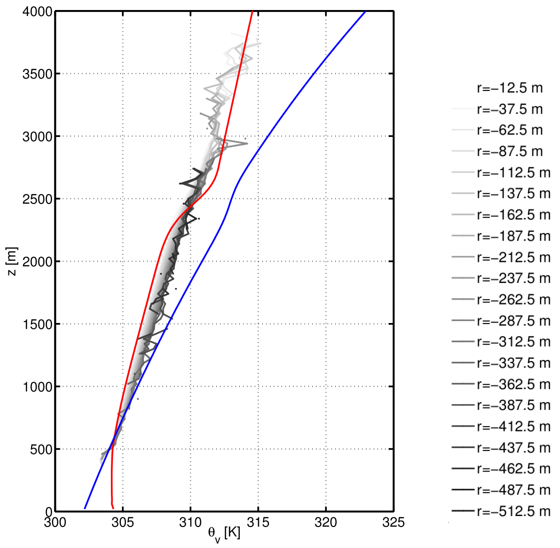

(a) Profile of θ_v for different r

FIG. 15: Virtual potential temperature profile for various values of distance to the cloud edge r. The red and blue lines represent the environmental and adiabatic profiles, respectively.

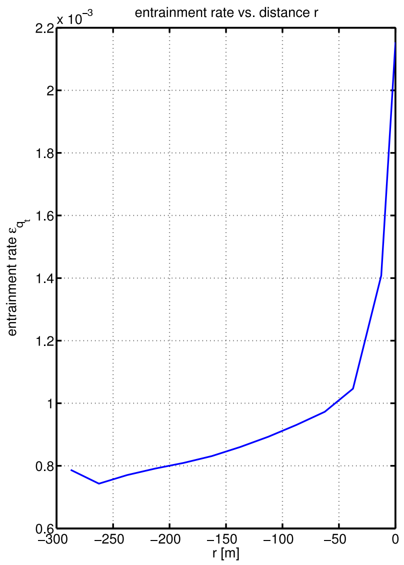

FIG. 16: Entrainment rate ε_{q_t} as function of r

It appears that indeed, the deeper inside the cloud, the smaller is the entrainment rate, but it is certainly not vanishing.

3.5 *Cloud Mixing*

How does the cloud exactly mix with its environment? This can be well studied by writing the mixing factor χ (e.g. de Rooy and Siebesma [2008]) as a function of the distance to the cloud edge r, as is done in section 2.1: equations (11) and (12). The results for different heights and $\chi(q_t(r))$ as well as $\chi(\theta_l(r))$ are shown in figure 17. It

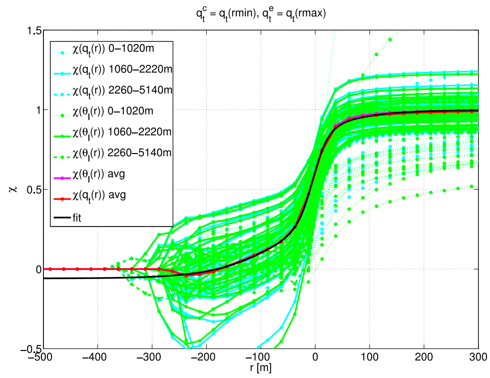

FIG. 17: Calculated $\chi(q_t(r))$ and $\chi(\theta_l(r))$ for different heights. Also the averages over height and the fit χ^{fit} are plotted

shows a very nice result. Using only the values of the geometric core (φ^c) and of the far environment (φ^e) gives a clear image of the mixing characteristics. It can be observed that most of the mixing occurs the cloud edge area, but also in the cloud (in the buoyant core) some mixing occurs. The negative values for χ are an artefact of the calculation method. The values inside and outside the cloud are defined as in equation (13), thus by using the value deepest inside the cloud, and the value furthest in the environment, for every height. As can be seen in for instance figure 5(b), the point deepest inside the cloud is not always the maximum value. Putting these values inside equation (11) leads to negative values of χ.

As can be seen in figure 17, the results for $\chi(q_t(r))$ and $\chi(\theta_l(r))$ do not differ significantly. This allows us to choose one of those datasets, in this case $\chi(q_t(r))$, and average these over height. Using this average we can create a fit $\chi^{fit}(r)$. Since the graph looks like a hyperbolic tangent function, but asymmetric, two hyperbolic tangent functions are used:

$$\chi^{fit}(r) = a_0 + a_1 \tanh\frac{r - r_1}{\lambda_1} + a_2 \tanh\frac{r - r_2}{\lambda_2} \quad (19)$$

With this fit we have the link between the mixing fraction χ and the distance to the cloud edge r and now we can write other quantities as a function of χ, like $q_l(r)$ and $\theta_v(r)$ according to the functions presented in section 2.1. It is interesting to compare the θ_v, constructed with the q_t^c, q_t^e, θ_l^c, θ_l^e values and the fit $\chi^{fit}(r)$, as defined in equation (17), with the original θ_v acquired from the LES run. This result is presented in figure 18. In this figure the excesses $\theta_v' = \theta_v - \overline{\theta_v}$ are averaged over height. This is done for both the constructed and the original values. The fluctuations are a more logical choice to average over height

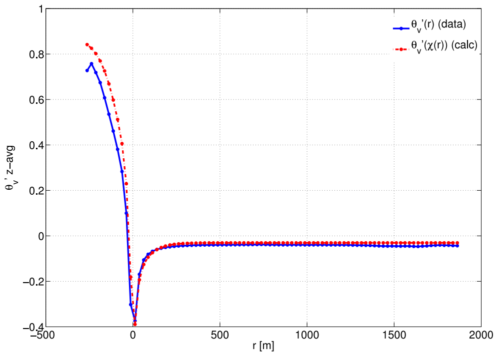

FIG. 18: Height averaged excesses of $\theta_v'(r)$ and of the constructed $\theta_v'(\chi(r))$

than the values itself. This appears to be a very good approximation of the $\theta_v'(r)$ and thus of $\theta_v(r)$.

From figure 17 it becomes clear that most of the mixing happens around the edge of the clouds. It even looks like it is a system that is mixing between three points. First, there is mixing along a straight line between the middle of the cloud and a point just inside the cloud. And secondly, there is mixing along a straight line between this last point and a point inside the shell. To verify this thought, an ensemble of 20 runs is used to look for this behavior in $\overline{\chi(q_t(r))}$, see figure 19.

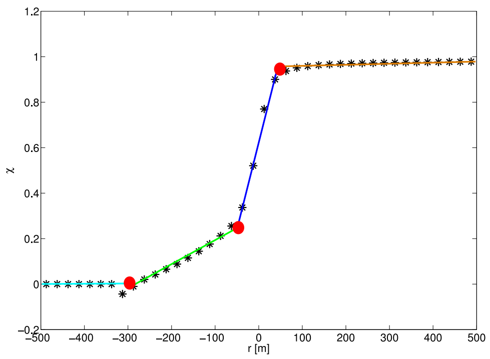

FIG. 19: Height averaged $\chi(r)$ for an ensemble of 20 runs with the three mixing points illustrated

4. CONCLUSIONS AND RECOMMENDATIONS

4.1 *Decomposition of the Cloud Edge Area*

The negative vertical velocity is the consequence of strong negative buoyancy
This is a confirmation of earlier findings. All other terms in the vertical momentum budgets are counteracting the downward motion in the shell.

The mass flux peak originates from the mass flux at the perimeters of medium-sized clouds
By using the cloud size diagnostics we were able to distinguish effects due to different sizes of a cloud. This led to the conclusion posted above. It appears that the perimeters of the largest clouds contribute the least, then the small clouds (either their cloud edges or their cores) and finally, most of the vertical transport of mass is done by the perimeters of the medium-sized clouds.

The environment is on average positively buoyant
It is observed by looking at the percentages, that in the environment 70% of the points is positively buoyant. Since it would be neutrally buoyant for 50%, this means that the far environment is on average positively buoyant. This result is consistent with the simple model by Heus and Jonker [2008].

4.2 *Cloud Edge Area Dimensions*

The strength of the shell is weakly correlated to the size of the cloud
By plotting the minimum value of the velocity outside the cloud versus the size of the corresponding cloud, a correlation can be seen between those two quantities. This can be explained by the observation that big clouds have strong cores. This was seen in the figure of the maximum velocity inside the cloud versus the cloud size. This upward movement has to be compensated by the downward velocity.

The width of the shell appears to be very weakly correlated to the size of the cloud
There are two figures that led to this result. First, the width of the shell versus the size of the cloud and second, the characteristics of the fit of the mixing factor versus the cloud size. This first graph suggested that the width is uniform for different cloud sizes, but the second shows a slight increase. It might be that the way the fit for χ has been set up is inherent to this result. The fit is constructed of two hyperbolic tangent functions. With a bigger cloud the asymmetry increases and thus the top of the derivative shifts to the left, increasing the σ_2 alongside.

4.3 *Properties of the Geometric Core*

The existence of undiluted cores inside shallow cumulus clouds is unlikely
When looking at the profiles of the quantities for different distances to the cloud edge, it is seen that even deep inside the cloud these profiles do not align with the adiabatic profiles that would be expected for undiluted cores. Together with the graph showing that the entrainment rate does not go to zero inside the cloud, this result leads to the conclusion that the existence of undiluted cores is not very likely. The whole cloud is dynamic and mixes with its environment. This mixing is damped with the distance further into the cloud but does not go to zero since the geometric core is still mixing with the area around it.

4.4 *Cloud Mixing*

The mixing factor χ can be linked to the cloud distance r
Calculating the mixing factor on the basis of q_t^c and q_t^e or on the basis of θ_l^c and θ_l^e and their profiles as a function of r leads to a relation between this cloud distance and the mixing factor χ. This relation at first sight looks like a hyperbolic tangent function, but taking a closer look suggests that there is a slight asymmetry that requires a second hyperbolic tangent function. With this relation it is shown that most of the mixing happens around the cloud edge.

The virtual potential temperature can be parametrized by the use of only the values of θ_l and q_t inside the cloud and the environment and with the relationship between χ and r
It is shown that when this relationship between χ and r is available, only the information of four points is needed to calculate the virtual potential temperature as a function of r. This works only in the middle of a cloud since at the top and bottom the relationship changes due to other effects not taken into account. The four points are θ_l^c, θ_l^e, q_t^c and q_t^e, defined as the furthest points available inside and outside the cloud.

The mixing between cloud and environment seems to occur in a three point mixing way
The first point is the geometric core of the cloud, the second is the point in the area close to the edge, but still inside the cloud and the final point is in the area just outside the cloud, the shell. It appears that straight lines can be drawn between those points to match the mixing profile $\chi(r)$. Some mixing still occurs outside this area, but this effect can be neglected.

4.5 *General Conclusion*

Based on the previous conclusions the following image of mixing in and around shallow cumulus clouds emerges. This image is illustrated in figure 20 and suggests that the cloud consists of three areas: a geometric core, a buoyant core and a region where most of the mixing takes place, near the cloud edge. Outside the cloud the shell is responsible for the mixing. In the figure the shell is illustrated by a oval which is a simplification of the reality. Further away, in the far environment, mixing effects are negligible. In this figure also the mixing points (as shown before in figure 19) are indicated.

ACKNOWLEDGMENTS

This work was sponsored by the National Computing Facilities Foundation (NCF) for the use of supercomputer facilities, with financial support of NWO. The authors like to thank Pier Siebesma and Stephan de Roode for their valuable input during the project.

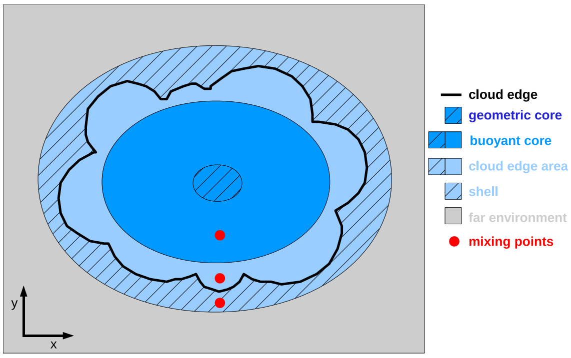

FIG. 20: Illustration of the formed image of a cloud in this thesis.

REFERENCES

W. C. de Rooy and A. P. Siebesma. A simple parameterization for detrainment in shallow cumulus. *Monthly Weather Review*, 136(2):560–576, 2008.

T. Heus and H.J.J. Jonker. Subsiding shells around shallow cumulus clouds. *J. Atmos. Sci.*, 65:1003 – 1018, 2008.

T.C. Heus, F.J. Pols, H.J.J. Jonker, H.E.A. van den Akker, and D.H. Lenschow. Observational validation of the compensating mass flux through the shell around cumulus clouds. *QJRMS*, 135:101 – 112, 2009.

P.R. Jonas. Observations of cumulus cloud entrainment. *Atmospheric Research*, 25:105 – 127, 1990.

H.J.J. Jonker, T. Heus, and P. P. Sullivan. A refined view of vertical transport by cumulus convection. *Geophys. Res. Lett.*, 35, 2008.

S.M.A. Rodts, P.G. Duynkerke, and H.J.J. Jonker. Size distributions and dynamical properties of shallow cumulus clouds from aircraft observations and satellite data. *J. Atmos. Sci.*, 60:1895 – 1912, 2003.

Y. Wang, B. Geerts, and J. French. Dynamics of the cumulus cloud margin: An observational study. *J. Atmos. Scie.*, 66(12):3660–3677, 2009.